

Solid-liquid equilibria in the ThO₂ – ZrO₂ system: An experimental study

Emtethal Hashem^a, Alice Seibert^a, Jean-François Vigier^a, Mohamed Naji^{a, 2}, Sara Mastromarino^{a, b, 1}, Andrea Ciccioli^b, Dario Manara^{a, *}

^a European Commission, Joint Research Centre (JRC), Directorate of Nuclear Safety and Security, P.O. Box 2340, D-76125, Karlsruhe, Germany

^b Università "La Sapienza", Department of Chemistry, Piazzale Aldo Moro 5, 00185, Rome, Italy

ARTICLE INFO

Article history:

Received 11 December 2018

Received in revised form

26 February 2019

Accepted 23 April 2019

Available online 30 April 2019

Keywords:

Melting

Mixed oxides

Thorium nuclear fuel

Thorium oxide

Zirconium oxide

ABSTRACT

In this work, solid-liquid equilibria of the pseudo-binary system ThO₂-ZrO₂ are investigated. A series of different molar ratios (80:20, 60:40, 40:60, and 20:80 ThO₂:ZrO₂) of ThO₂ and ZrO₂ were synthesised at JRC-Karlsruhe using an external sol-gel method. The XRD data of samples sintered at 1650 °C show two-phase behaviour throughout the range of compositions with small solubility (<5%) of ZrO₂ in ThO₂ and limited solubility of ThO₂ in ZrO₂. These results were supported with Raman spectroscopy and SEM measurements to have a better understanding of the distribution of the components within each other. Solid/liquid equilibria in the ThO₂-ZrO₂ system are investigated here for the first time by laser heating coupled with fast optical thermometry under a controlled atmosphere. A minimum solidus point exists in this system for intermediate compositions (close to Th_{0.4}Zr_{0.6}O₂) at approximately 2750 K. These results contribute to assessing the thermal stability of the fuel-cladding system in a ThO₂-fuel based reactor. Moreover, when compared with other similar mixed oxide systems, the present data confirm the essential role played by oxygen chemistry in the definition of the studied phase boundaries.

© 2019 The Authors. Published by Elsevier B.V. This is an open access article under the CC BY license (<http://creativecommons.org/licenses/by/4.0/>).

1. Introduction

The ThO₂-ZrO₂ system is of great interest in the framework of severe accident investigation principally because Light Water Reactor (LWR) could be loaded with thorium dioxide-based fuel in a Zircaloy cladding [1]. In addition, Th-based fuels can also be used as an inert matrix fuel for the transmutation of long-lived radionuclides, aimed at reducing the long-term radiotoxicity of spent fuel [2]. The use of thorium dioxide as a nuclear fuel has other interesting implications as waste management and operating conditions can be improved compared to other actinide-dioxide-based fuel [1–7]. Thorium dioxide mixed fuels have also advantages with respect to proliferation resistance for nuclear weapons,

although this point is still rather controversial [8]. Thorium dioxide is also of interest for its fundamental chemical and physical properties [9]. It is indeed a very stable oxide, not subject to oxidation as uranium dioxide is, although a slight tendency to reduction at very high-temperature (above 3000 K) was reported [10]. Its reported melting temperature occurs beyond 3600 K [10,11], which makes thorium dioxide the highest melting oxide known. The chemical stability and the high melting temperature present potential advantages for the fuel performance of thorium fuel and its safety.

The quasi-containerless laser heating technique under controlled atmosphere used in this work is particularly suited for the study of very-high melting compounds. It has been used, in the last decade, for the study of pure and mixed refractory compounds of interest for nuclear, aerospace and geological applications [12–16].

In this research, the melting behaviour of the ThO₂-ZrO₂ system is studied experimentally with this technique for the first time. Previously, such melting behaviour was studied only once, with the help of a solar furnace heating technique [17]. Results are discussed and compared with the more extensively investigated solid-liquid equilibria in the system UO₂-ZrO₂. Such comparison sheds some light on the peculiar behaviour of uranium-containing mixed

* Corresponding author.

E-mail address: dario.manara@ec.europa.eu (D. Manara).

¹ Current address: Nuclear Energy and Radiation Applications (NERA), Radiation, Science & Technology Department, Faculty of Applied Sciences, Delft University of Technology, Mekelweg 15, 2629, JB Delft, the Netherlands.

² Current address: Physics Department, Faculty of Sciences Dhar Mehraz, Laboratory of Applied and Theoretical Physics, University Sidi Mohamed ben Abdellah, B.P. 1796, Atlas Fez, Morocco.

oxides with respect to other similar actinide oxide systems.

2. Experimental

2.1. Sample preparation

Five compositions with different $\text{ThO}_2/(\text{ThO}_2+\text{ZrO}_2)$ molar fractions (1.00, 0.80, 0.60, 0.40, 0.20) were prepared at JRC Karlsruhe, as summarised in Table 1. The mixed $\text{ThO}_2\text{-ZrO}_2$ oxide materials were prepared by a sol-gel assisted precipitation technique deployed at JRC Karlsruhe [18]. Feed solutions with fixed $\text{ThO}_2/\text{ZrO}_2$ molar ratios of nominally 100/0, 80/20, 60/40, 40/60, 20/80 were prepared from stock solutions of thorium nitrate hydrate $\text{Th}(\text{NO}_3)_4 \cdot x\text{H}_2\text{O}$, and zirconyl chloride, ZrOCl_2 in distilled water. The mixed solutions were checked with Inductively Coupled Plasma Mass Spectrometry (ICP-MS) to determine the final metal content. ICP-MS analysis was executed with a Thermo Finnigan Element2 instrument adapted to a glovebox. Table 1 summarizes the results of these measurements. The slight discrepancy to the nominal values may be explained by the use of highly concentrated stock solutions of Th and Zr salts which were not checked for their concentration before the aliquots for the mixed solutions were taken. Routinely these freshly prepared mixed solutions are used to determine the composition of the feed solutions which is assumed to prevail also in the solids due to similar precipitation behaviour of Th and Zr confined in the sol-gel matrix.

For convenience in the text and graphs the nominal composition values are used.

Following the addition of a surface-active agent and organic thickener, the solution was dispersed into droplets using a hand-held electronic pipette. The droplets were collected in an ammonia bath, where gelation occurs. After ageing for 24 h, the resulting spheres were washed with distilled water and dried in air for 24 h. Calcination was carried out over three steps in order to slowly remove excess water and organic material from the sol-gel process. Calcination was done at 373 K for 2 h followed by 673 K for 2 h and finally at 973 K for 4 h in air. To obtain pellets the powder material was pressed and sintered. Conventional pressing to pellets was obtained with a uniaxial press using a 7.1 mm matrix and a load of 15 kN. Sintering conditions were 6 h at 1923 K under an argon flow, with temperature ramps of 200 K/h for heating and cooling step on a molybdenum tray. These sintering conditions usually do not induce any hypostoichiometry in the pure oxides ThO_2 and ZrO_2 but keep the stoichiometry at 2.0. as corroborated also by the XRD results of the sintered samples, reported in later sections of this paper. It is assumed that also the mixed compositions are stoichiometric under the applied sintering conditions. Indeed, all samples showed no distinct blackening as observed for example in ZrO_2 or Ca oxide samples usually ascribed to oxygen defects.

2.2. Laser heating and temperature measurement techniques

Laser heating combined with fast pyrometry is the experimental approach employed in this work. It is particularly suited for the study of ultra-refractory oxides like ThO_2 and ZrO_2 . Details of the

laser-heating setup used in this research have been reported in previous publications [12,14,15].

Thermograms were measured by sub-millisecond resolution pyrometry on mixed $\text{ThO}_2\text{-ZrO}_2$ samples laser heated beyond melting by a TRUMPF® Nd:YAG cw laser radiating at 1064.5 nm. Its power vs. time profile is programmable with a resolution of 1 ms. Laser shots of different duration (from a few tens to a few hundred ms) and laser power density (300 W cm^{-2} to 3000 W cm^{-2}) were repeated on the same 3-mm to 8-mm diameter spot on a single sample surface as well as on different samples of the same composition in order to obtain statistically significant datasets for each composition and heating cycle.

During the shots, the investigated specimen was held in a sealed autoclave under a controlled atmosphere. In a first series of experiments, the atmosphere was chosen on the basis of thermodynamic equilibrium calculations between the condensed phases and the vapour, in order to maintain as much as possible the original composition of each sample throughout the heating/cooling cycles. Thus, both ThO_2 -rich samples and ZrO_2 -rich ones were first studied under dry compressed air (at 0.3 MPa), in order to minimise oxygen losses from the condensed phases. Successively, laser heating tests were carried out under an inert/reducing atmosphere (pressurised argon at 0.3 MPa), in order to study the solidus-liquidus behaviour of the present samples in a situation favourable to the formation of oxygen defects in the condensed material.

It is worth pointing out here that, as far as the material safety is concerned, melting onset or complete solidification are the important phenomena, because they imply a first-order change in the mechanical stability and other relevant properties of the material itself. Technically, melting onset and complete solidification of a mixed material (solid or liquid solution) correspond to the solidus temperature. However, it was shown in recent research [e.g. 15] that under the current laser heating conditions, and in general in the rapid heating/cooling regimes that can occur during a nuclear core meltdown transient, the melting/solidification onset temperatures can be slightly higher or lower than the thermodynamic solidus. This effect is due to moderate deviations for the thermodynamic equilibrium, occurring when mass diffusion rates become comparable with the heating and cooling rates. Taking into account the current experimental uncertainties, the temperatures of melting onset and final solidification can be safely identified with the solidus point of a given composition.

In this kind of experiments, thermal shocks are usually minimised by applying a pre-heating level around 1500 K to limit thermal stresses due to the extreme laser power density impinging on the surface of the sample [14,18,20]. This procedure, consisting of heating the sample at that temperature before starting the actual high-power pulses, was difficult to apply to the current oxides, due to their semi-transparent behaviour. White oxides like ThO_2 and ZrO_2 are largely transparent to near-infrared (NIR) radiation (as in the heating laser used here) at room temperature and up to the temperature at which an optical transition occurs, following which they absorb 80%–90% of the infrared radiation. Such a transition typically occurs between 1800 K and 2500 K. Such an optical behaviour, linked to the value of the gap between valence and conduction electronic bands [11], is common in white oxides [21], hence the nomenclature “semi-transparency”. It constitutes a real difficulty for the laser heating of white oxides. In fact, a very large NIR laser power density is needed to heat the samples up to the optical transition temperature. However, as soon as the latter is attained, a much smaller power density is sufficient to heat samples well beyond their melting (solidus) point, or to shatter them before one can take any actual measurements of their properties. In this situation, laser power profiles suited to the present samples could be obtained only by a challenging trial-and-error procedure and by

Table 1
Initial composition of the five $\text{ThO}_2\text{-ZrO}_2$ feed solutions analyzed by ICP-MS.

Anticipated Sample	Actual mol% ThO_2	Actual mol% ZrO_2
ThO_2	100	0
$\text{Th}_{0.8}\text{Zr}_{0.2}\text{O}_2$	81.86	18.14
$\text{Th}_{0.6}\text{Zr}_{0.4}\text{O}_2$	64.40	35.60
$\text{Th}_{0.4}\text{Zr}_{0.6}\text{O}_2$	45.14	54.86
$\text{Th}_{0.2}\text{Zr}_{0.8}\text{O}_2$	23.62	76.38

using the possibility to programme a sequence of laser heating pulses. Once heated beyond the optical phase transition, during the series of four heating-cooling cycles on the same sample spot the material was never cooled below it, in order to avoid further thermal shocks. The duration of the high-power pulses was increased from one heating-cooling cycle to the other, in order to check the repeatability of the results under slightly different experimental conditions (Fig. 1). This approach ensured a better mechanical stability of the samples, over which several successive shots could be repeated to check the result reproducibility and the eventual effects of non-congruent vaporisation or segregation phenomena. The onset of melting (solidus point for mixed compositions) was detected by the appearance of vibrations in the signal of a probe laser (Ar⁺ cw 750 mW to 1.5 W) reflected by the sample surface (Reflected Light Signal technique, or RLS). The sample cooled naturally when the laser beam was switched off during the thermal cycle. Thermal inflections corresponding to the first formation of solid crystals in the liquid (liquidus) and thermal arrests corresponding to complete solidification (solidus) were then observed on the thermograms recorded by the fast pyrometers, operating in the visible-near infrared range between 488 nm and 900 nm. The reference pyrometer wavelength was 655 nm and was calibrated according to the procedure already reported elsewhere [15]. Direct measurement of the sample thermal emission yielded the radiance temperature at the pyrometer wavelength. The real sample temperature was obtained from the radiance temperature using the following pyrometry equation, which can be easily derived from Planck's radiation law corrected with the normal spectral emissivity, ϵ_λ :

$$\frac{1}{T} = \frac{1}{T_\lambda} + \frac{\lambda}{c_2} \ln \epsilon_\lambda(\lambda, T) \quad (1)$$

Equation (1) is valid within Wien's approximation to Planck's law, i.e. when $\exp\left(\frac{c_2}{\lambda \cdot T}\right) > 1$.

If λ is expressed in μm and T in K, then the universal constant c_2 takes the value of $14388 \mu\text{m K}$.

The normal spectral emissivities (ϵ_λ or NSEs) of thoria and zirconia beyond the NIR transparent/opaque transition temperature are assumed as 0.87 and 0.9, respectively, as determined from previous work [12]. Values of intermediate compositions have been obtained by linearly interpolating the two end member values

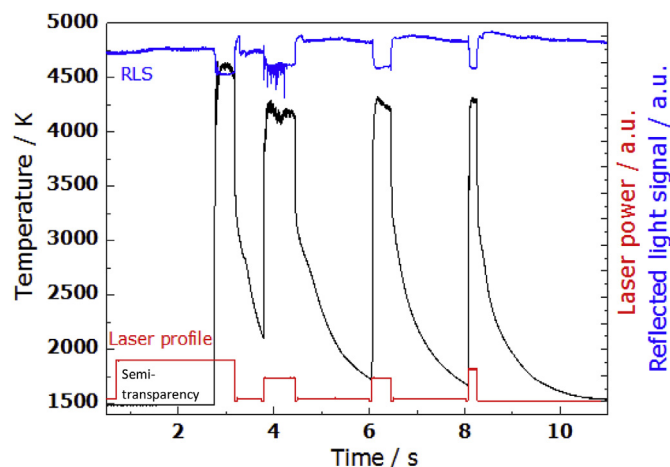


Fig. 1. A sequence of four laser heating pulses performed on $\text{Th}_{0.6}\text{Zr}_{0.4}\text{O}_2$ in air. Reflected light signal represented by the blue line identifies the existence of liquid on the sample surface. (For interpretation of the references to colour in this figure legend, the reader is referred to the Web version of this article.)

according to the volume fraction of each component. The latter was considered to provide the best estimate of the surface fraction averaged over all the possible grain orientations. These NSE values have been cross-checked in the current work with the help of a multi-wavelength spectro-pyrometer. This approach, similar to that reported in Ref. [14], consists in the measurement, during the current heating cycles, of the thermal emission (or radiance) spectra of the sample. Non-linear minimum-square fit of such spectra, using Planck's equation corrected for the normal spectral emissivity, yield values for real temperature and NSE throughout the heating/cooling cycles, although with a more limited time resolution than the single-channel pyrometer.

Uncertainty of the measurements were calculated according to the error propagation law [15], taking into account the uncertainty associated to pyrometer calibration, the emissivity, transmittance of the optical system and the accuracy in detecting the onset of vibrations in the RLS signal. The estimated cumulative uncertainty is thus $\pm 1\%$ of the reported temperatures in the worst cases, with a 1- σ coverage factor (corresponding to one standard deviation around the average value).

2.3. XRD analysis

The crystallographic structure of the materials was determined at room temperature by X-Ray diffraction using a Bruker D8 X-ray diffractometer mounted in a Bragg–Brentano configuration with a curved Ge monochromator (1,1,1), a copper tube (40 kV, 40 mA) and equipped with a LinxEye position sensitive detector. For the measurement, the ground powders were deposited on a silicon wafer to minimize the background and dispersed on the surface with 2 or 3 drops of isopropanol. Structural analyses were performed with the JANA 2006 software suite [22] by the Le Bail method. Only the profile fitting is used with predefined phases, as no unknown phases were obtained.

2.4. Scanning electron microscopy

A Philips XL40 scanning electron microscope (SEM) operated at 20 kV and installed in a glove box was employed in the present research. Quantitative Energy Dispersion Spectrometry (EDS) analysis and X-ray element maps were acquired, using a shielded Cameca SX100R electron microprobe.

2.5. Raman spectroscopy

Raman measurements were performed using a Raman microscope equipped for the present measurements with a long working distance (10.6 mm) objective which offers a 0.5 numerical aperture with a $\times 10\text{k}$ or $\times 50\text{k}$ magnification. The Raman spectroscopy is a Jobin-Yvon T 64000 equipped with an 1800 grooves-per-mm grating, a low noise liquid N_2 cooled Symphony CCD detector and edge filters blocking the elastic scattering coming from the sample. Excitation sources are an Ar⁺ or a Kr⁺ Coherent[®] CW laser with main wavelengths at 514 and 647 nm, respectively, and a controllable nominal power up to 400 mW. The power impinging the sample surface is lower by a factor 5 approximately. Using the long focal $\times 50\text{k}$ objective and the single spectrometer mode permits a good spectral resolution ($\pm 0.5 \text{ cm}^{-1}$) was obtained independently of the surface shape. The spectrograph is calibrated with the T_{2g} excitation of a silicon single crystal, set at 520.5 cm^{-1} [23]. The instrument is calibrated on a daily basis prior to measurements.

3. Results

3.1. Laser heating

Typical thermograms obtained by the laser melting – fast pyrometry setup are shown Fig. 1. As already stated, it is extremely difficult to melt thorium, due to the high melting temperature and its initial transparency to the laser wavelength. At the beginning of the first thermogram of the series reported in Fig. 1 one can see the semitransparency effect on the temperature profile. Because of this particular optical behaviour, a first higher-power and high-energy laser pulse was used to rapidly overcome the “semitransparent plateau”. At the end of this step, lower power laser pulses were sufficient to heat a ThO₂ sample beyond the melting point.

When the laser pulses were switched off, the temperature dropped and thermal arrests could be detected corresponding to first-order liquidus and solidus phase transitions. Different heating cycles were performed on the same samples with varying power intensities. In this way, it was checked that the samples were stable for numerous laser heating cycles, during which the recorded thermal arrest temperatures were hardly influenced by potential segregation effects. Fig. 2 shows a magnification of the cooling stage of a thermogram recorded on a Th_{0.6}Zr_{0.4}O₂ sample in pressurised Argon. After a clear effect of the vapour plume formed at high temperature, the first marked inflection on the thermogram is due to the latent heat released at the liquidus temperature where the first solid seeds nucleate from the molten mass.

The solidus point is identified as the lowest-temperature thermal arrest in the thermogram, which also corresponds to the termination of the last large oscillations in the RLS not correlated to noise. Such oscillations are linked to assessment movements of the liquid surface, to convective motions in the liquid, and, at very high temperature, to boiling [14,24]. These phenomena are obviously related to the density of the liquid and its surface tension. In some cases, like in the example reported in Fig. 2, such changes are better observed in the first derivative of the RLS. It should be noted here,

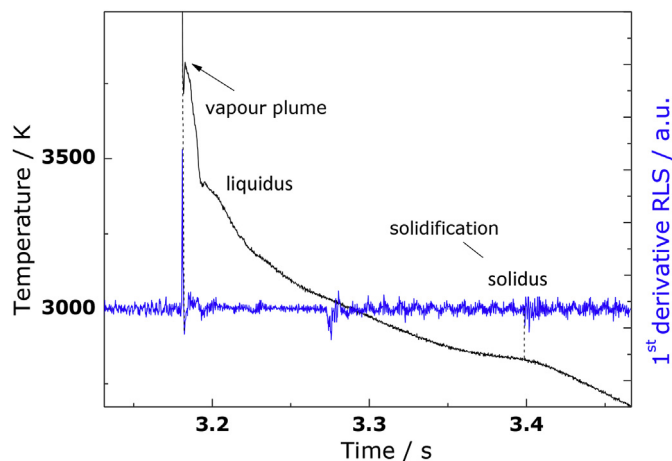


Fig. 2. Magnification of the cooling flank of a thermogram recorded on a Th_{0.4}Zr_{0.6}O₂ sample in pressurised argon. The liquid/solid transition occurs in two steps (liquidus, solidus), corresponding to separated inflections on the cooling curve. A higher-temperature dip in the thermogram corresponds to the condensation of a vapour plume on the sample surface, which can be used as an approximate indication of the boiling temperature. The solidus point is identified as the lowest-temperature thermal arrest in the thermogram, which also corresponds to the last large oscillations in the RLS not correlated to noise. It should be noted here, that noise-related oscillations in the RLS are easily distinguishable as a regular sinusoidal signal in the RLS derivative. Irregular oscillations are related to the presence of a liquid phase on the sample surface, and disappear below the solidus temperature.

that noise-related oscillations in the RLS are easily distinguishable as a regular sinusoidal signal in the RLS derivative. Irregular oscillations are related to the presence of a liquid phase on the sample surface, and disappear below the solidus temperature. The change of the signal observed before the thermal arrests is probably linked to large vapour release at high temperature, which occasionally resulted, upon cooling, in a white deposit on the autoclave window. In principle if this condensation happened on the optical path of the pyrometers, it could affect the temperature measurements, resulting in an additional uncertainty on the measured transition points. Since this condensation effect has been observed only occasionally, the corresponding additional uncertainty is considered to be at least partially represented by the data dispersion standard deviation reported in Table 2.

This effect was more relevant at very high temperatures (beyond 3000 K), where vaporisation is expected to be more intense. This explains the apparently low melting temperature recorded here for pure ThO₂, compared with most literature data [11,12]. It should be noticed, nonetheless, that also the melting temperature reported for ThO₂ by Böhler et al. [12] is affected by a large uncertainty, most probably related to the same vaporisation phenomena.

Table 2 summarizes the solidification temperatures observed for the different compositions.

The solidus temperature for pure ThO₂ in this work is measured as 3444 K in argon and 3559 K in air. The value measured in air is not far, considering the uncertainty bands, from the melting point of 3624 K ± 86 K reported by Böhler et al. [12], and from the 3651 K ± 17 K by Ronchi and Hiernaut [11]. The latter literature values are closer to inflections observed in the present thermograms and identified, with the help of RLS, as liquidus points. In this context it is pertinent to point out that the uncertainties reported in literature data are not only instrumental, but they can also be linked to the sample, the heating rates and potential liability of the sample to go substoichiometric in oxygen, which would indeed result in splitting the solidification process into a liquidus and a solidus. Independently of that, a deviation of 110 K around the melting point measured in argon and air is shown in Table 2 for the sample of pure ThO₂. This large difference can be due to the vaporization effect described above, which in ThO₂-ZrO₂ samples was more abundant in an inert-reducing atmosphere than in an oxidizing one. It is in fact clear that an oxidizing atmosphere can compensate oxygen losses, and better stabilize the condensed dioxide phases (solid or liquid). The sample Th_{0.8}Zr_{0.2}O₂ also presents a deviation of 130 K between the melting temperatures recorded under the different atmospheres. The same behaviour is not observed for the compositions richer in ZrO₂. This behaviour might look strange when one considers that thorium is one of the most stable dioxides in nature. Thorium remains always in the oxidation state (IV) in it so as most Zr in zirconia. However, large vaporisation and oxygen losses do occur at very high temperatures. In the case of thorium, more than a reduction from Th⁴⁺ to Th³⁺—very unlikely even at high temperature—, one could expect the formation of metallic thorium behind the observed difference between the melting points in air and in argon. Traces of metallic thorium were in fact observed by XRD analysis in the sample of pure thorium after melting in a reducing atmosphere (Fig. 3). The Th–O phase diagram optimised by Benz [10] and recently reassessed by Bergeon et al. [25], actually shows that metallic Th can be demixed upon rapid solidification of ThO₂ in case oxygen losses occur at high temperature. After comparing this result with the data previously obtained for the UO₂-ZrO₂ system [26], one can certainly infer that the hyperstoichiometric oxides formed in the uranium richer compositions melted in air are related to oxidation state changes occurring in urania only, as the current result corroborate again the

Table 2
Solidification points recorded on the current ThO₂ – ZrO₂ samples.

Sample	Reducing atmosphere (Ar)			Oxidizing atmosphere (air)		
	Liquidus T/K	Solidus T/K	Uncertainty/K	Liquidus T/K	Solidus T/K	Uncertainty/K
ThO ₂	3630	3444	7	3625	3559	53
Th _{0.8} Zr _{0.2} O ₂	3550	3277	22	3554	3403	61
Th _{0.6} Zr _{0.4} O ₂	3323	3320	20	3325	3050	80
Th _{0.4} Zr _{0.6} O ₂	3022	2749	12	2778	2778	28
Th _{0.2} Zr _{0.8} O ₂	3020	2783	4	2796	2796	3.5
ZrO ₂	NA	NA	NA	2970	2970	30

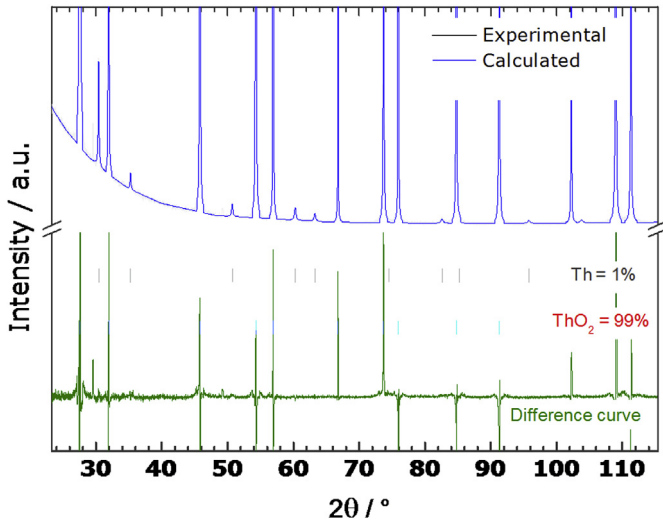


Fig. 3. XRD pattern of a ThO₂ sample laser melted and quenched in pressurised argon. A small fraction of metallic Th was segregated during quenching.

inertness of the ZrO₂ towards further oxidation.

From the current data, plotted in Fig. 4 as a function of the initial sample composition, a minimum melting point can be interpolated for a composition close to Th_{0.4}Zr_{0.6}O₂ and a temperature of approximately 2750 K. It should be noted, incidentally, that the measurement of this minimum melting temperature, more than

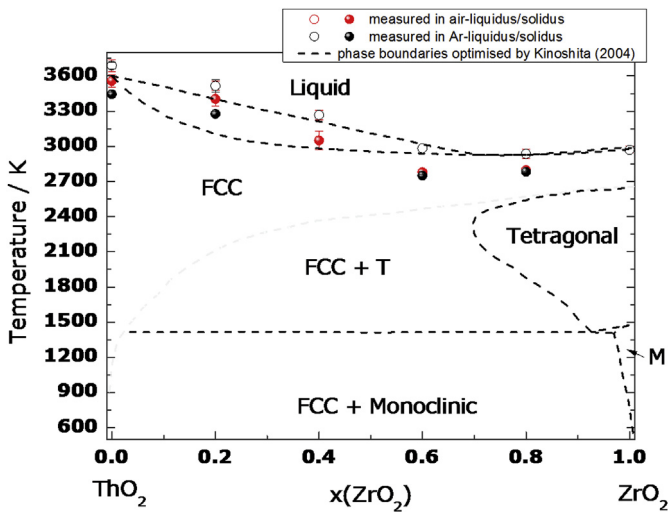


Fig. 4. The solidus and liquidus points obtained in this work in the ThO₂-ZrO₂ system, compared with the CALPHAD-optimised phase boundaries obtained by Kinoshita et al., in 2004 [9].

800 K lower than the liquefaction point of pure thoria, was little affected by the aforementioned vaporisation, due to the lower Th content in the sample.

The molten sample surface remained white in laser heating experiments carried out under pressurised air. In contrast, under compressed argon the samples tended to become black. In case of pure thoria, the colour change may also be due to metallic inclusions in ThO₂. This change in colour has been observed in several oxides (e.g.: CaO, CeO₂, ZrO₂) [19,21] that look darker when oxygen defects are formed, and lighter grey or white when they are defect-free at room temperature. They are actually transparent (or semi-transparent, insofar as this effect disappears at high temperature), and look white because of the different orientations of crystallites in poly-crystals, which diffuse light in all directions. The formation of oxygen defects (vacancies, interstitials) promptly increases the visible light absorption, resulting in a darker colour. In the current samples, oxygen defects are formed at high temperature more easily in an inert atmosphere than in an oxidising one [19].

3.1.1. SEM

The samples as used for melting point measurement (after sintering process) were analyzed by scanning electron microscopy at different magnifications. A back-scattering electron microscope image in Fig. 5 shows the surface of a sample after melting. The brighter parts are related to compositions richer in ThO₂ whilst darker parts are richer in ZrO₂. EDX analysis showed no change of composition along the surface within the instrumental uncertainties ($\pm 10\%$ in composition). The measured compositions, averaged in Table 3, were in qualitative agreement with the ICP-MS data reported in Table 1.

This agreement shows that no compositional segregation

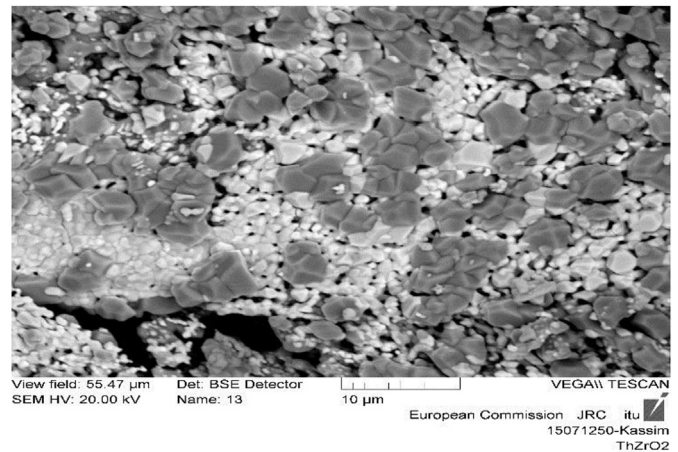


Fig. 5. Back-scattered electron image obtained with a VEGA_TESCAN Scanning Electron Microscope on a Th_{0.4}Zr_{0.6}O₂ sample melted and quenched in pressurised argon.

Table 3
EDX-measured average compositions of the five ThO₂-ZrO₂ feed solutions analyzed by ICP-MS.

Nominal composition	ICP-MS of initial sample	Average EDX composition of the laser-melted surface
Th _{0.8} Zr _{0.2} O ₂	Th _{81.86} Zr _{18.14} O ₂	Th _{85.03} Zr _{14.97} O ₂
Th _{0.6} Zr _{0.4} O ₂	Th _{64.40} Zr _{35.60} O ₂	Th _{62.70} Zr _{37.30} O ₂
Th _{0.4} Zr _{0.6} O ₂	Th _{45.14} Zr _{54.86} O ₂	Th _{38.44} Zr _{61.56} O ₂
Th _{0.2} Zr _{0.8} O ₂	Th _{23.62} Zr _{76.38} O ₂	Th _{21.51} Zr _{78.49} O ₂

occurred during the laser heating cycles, besides the aforementioned oxygen defect formation which could in any case not be detected by EDX or ICP-MS.

3.1.2. Raman spectroscopy

Possible segregation phenomena occurring during the laser heating-induced phase transitions were studied by Raman spectroscopy. Raman spectra were recorded in this work with an Ar⁺ 514 nm laser excitation source, which was found to be the wavelength producing the best Raman signal/noise and fluorescence ratio for the present materials. Measurements were conducted on the surface of the sample on as-sintered (not laser heated) and laser-heated/quenched material. Fig. 6 shows Raman spectra of all the compositions after sintering and before the laser heating cycles. The T_{2g} Raman active vibration of ThO₂ dominates the spectrum at 465 cm⁻¹. This triply degenerate T_{2g} peak is common for all the fluorite-like structures (fcc, Fm-3m) [27]. With increasing content of zirconium dioxide, the spectra present more and more the typical vibrational modes of monoclinic zirconia. A full list of all the vibrational modes of monoclinic and tetragonal zirconium dioxide is reported in Table 4. A precise line assignment can be found in Refs. [30,31]. An overlap is well visible in Fig. 6 between the T_{2g} peak at 465 cm⁻¹ in pure ThO₂ and one similar mode, which is attributed to an A_g vibration in monoclinic ZrO₂ [29,30]. For the as-sintered mixed compositions ThO₂-ZrO₂, the T_{2g} -A_g peak is located between 468 cm⁻¹ and 475 cm⁻¹ depending on the composition. The position of this latter feature is shown more in details in the inset of Fig. 6. It should be noted that, because of the immiscibility of cubic ThO₂ and monoclinic ZrO₂, the apparently single T_{2g} peak in the mixture is in reality the overlap of two separate and independent modes of vibration.

Raman spectra measured after melting of the samples show a variation in the fingerprint of the crystal, the coexistence of various

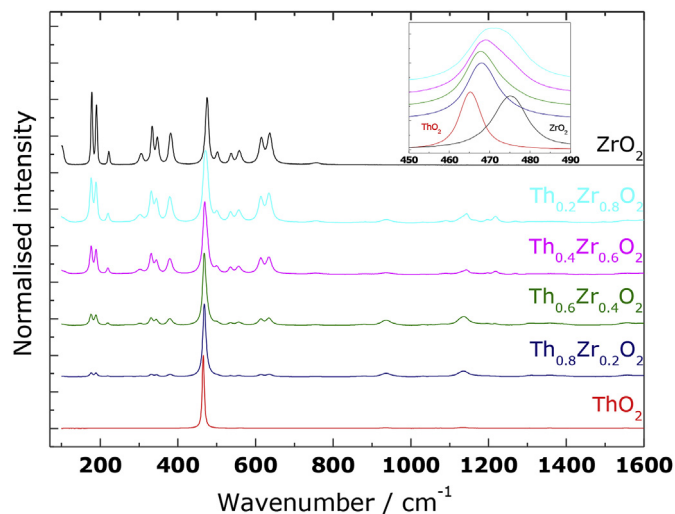


Fig. 6. Raman spectra recorded with a 514 nm Ar⁺ laser excitation source of the as-sintered ThO₂-ZrO₂ samples studied in this work.

Table 4
Raman assignment of the vibrational modes of ZrO₂.

Raman shift/cm-1	Assignment	References
103	Monoclinic ZrO ₂	[28–30]
148	Tetragonal ZrO ₂	
180	Monoclinic ZrO ₂	
192	Monoclinic ZrO ₂	
224	Monoclinic ZrO ₂	
263	Tetragonal ZrO ₂	
308	Monoclinic ZrO ₂	
335	Monoclinic ZrO ₂	
349	Monoclinic ZrO ₂	
383	Monoclinic ZrO ₂	
476	Monoclinic/tetragonal ZrO ₂	
503	Monoclinic ZrO ₂	
539	Monoclinic ZrO ₂	
561	Monoclinic ZrO ₂	
617	Monoclinic ZrO ₂	
638	Monoclinic ZrO ₂	
755	Monoclinic ZrO ₂	

phases, and an increased disorder. Fig. 7a and b show the Raman spectra collected on samples resolidified in reducing (a) and oxidising (b) atmosphere. No relevant difference is present for the compositions richest in thorium dioxide (i.e. Th_{0.8}Zr_{0.2}O₂), compared to the as-sintered samples. Compositions richer in zirconium dioxide and pure ZrO₂ show vibrational modes similar to the three Raman active modes typical of tetragonal zirconium dioxide [29,30], which is ensured by the Factor Group Analysis. The metastable tetragonal phase can be locally quenched to room temperature following heat treatments (laser heating).

In this system the quenching of a tetragonal phase in the laser heated samples is clearly observed with the help of the current Raman spectra. This is the main result of the post-melting Raman analysis reported in Fig. 7a and b.

Other spectral features are more complex in the quenched samples, certainly due to the abundant formation of oxygen defects which make Raman peaks broader and more difficult to analyse. A more detailed analysis of the present Raman spectra is beyond the scopes of the present research.

Fig. 8 presents the T_{2g} peak position for all the composition studied in this work as a function of the ZrO₂ content. The T_{2g}/A_g/E_g peak position for as-sintered samples (black symbols) is characteristic for each composition and the shift in the peak position displays a regular dependence on the ZrO₂ content of the samples. A shift of this peak is also present for the samples melted in air and in argon. In the latter two cases, however, the evolution of the peak position is less regular, with an apparent maximum at intermediate compositions, which may reveal the formation of oxygen defects resulting in broadening and shifting of both the ThO₂ and the ZrO₂ Raman lines.

3.1.3. X-ray diffraction

The initial powders were produced using sol-gel co-precipitation method which is known to give homogeneous starting material [18]. After calcination at 973 K, XRD showed that no thorium and zirconium oxide separation occurred, whereby a metastable

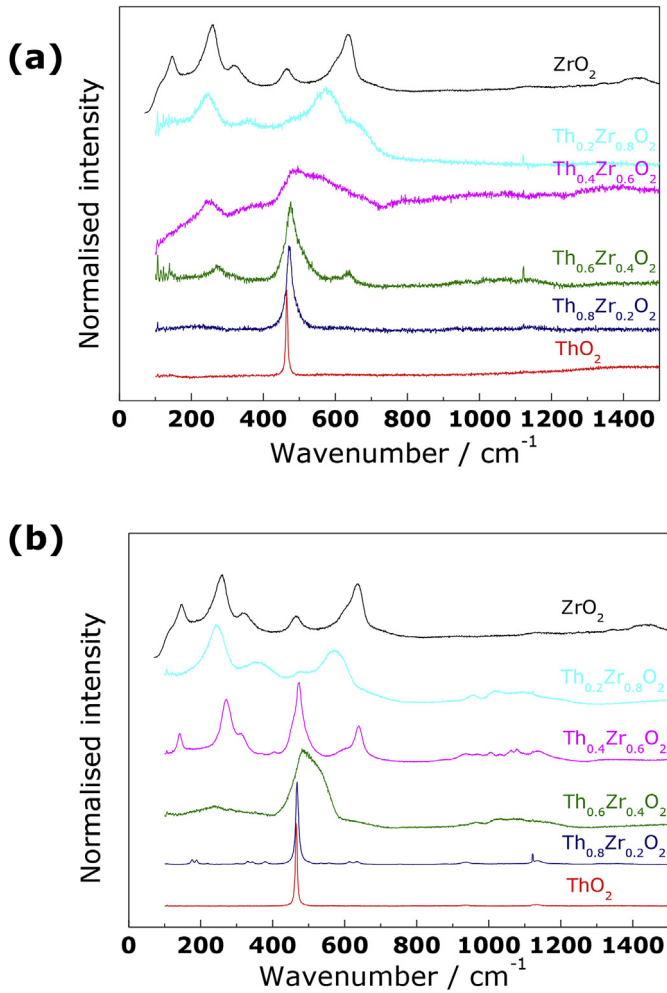


Fig. 7. Raman spectra recorded with a 514 nm Ar⁺ laser excitation source of the melted and quenched ThO₂-ZrO₂ samples studied in this work: a) in pressurised argon and b) in pressurised air. Quenching of a tetragonal phase in the laser heated samples is clearly observed. This is the main result of the post-melting Raman analysis. Other spectral features are more complex in the quenched samples, certainly due to the abundant formation of oxygen defects which make Raman peaks broader and more difficult to analyse.

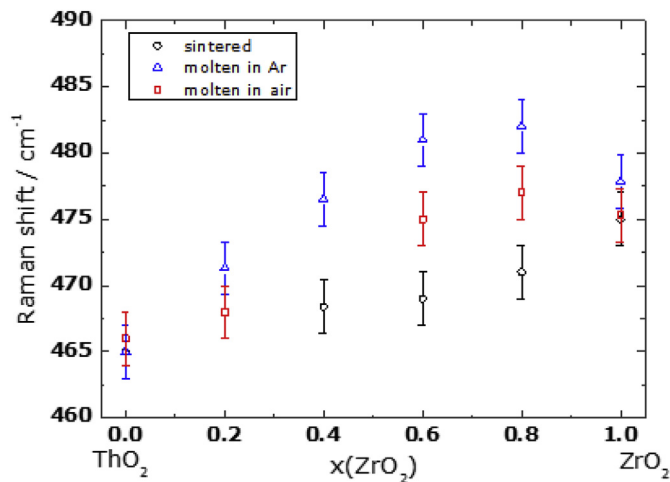


Fig. 8. The Raman T_{2g}/A_g/E_g peak position recorded in this work as a function of zirconia fraction in the current ThO₂-ZrO₂ oxides, after simple sintering, melting in pressurised argon and melting in pressurised air.

Th_{1-x}Zr_xO₂ solid solution was formed. The material was composed by single fluorite phase material having poor crystallinity and a lattice parameter decreasing with increase of zirconium content. Also Raman spectroscopy was performed on the calcined materials. The few, poorly defined and broad Raman bands recorded were nonetheless sufficient to confirm that calcined samples were single-phased and poorly crystalline. XRD patterns and Raman spectra recorded on the calcined material prior to sintering are reported in the Supplementary Material at the end of the paper. During the sintering step at 1923 K, demixing of the material into ThO₂ and ZrO₂ phases did occur. A mixture of cubic ThO₂ and monoclinic ZrO₂ is clearly identified through XRD, in good agreement with Raman and SEM observations, and with ThO₂-ZrO₂ phases diagram at room temperature (Fig. 4). The lattice parameters of the cubic and the monoclinic phase are not affected by the cationic composition in the mixtures (Table 5). However, there is a small but significant deviation from pure ThO₂ and pure ZrO₂ lattice parameters, suggesting trace of zirconium in ThO₂ phase and vice versa. As observed with Raman spectrometry, new metastable phases are visible through XRD after melting experiments, due to material quenching from temperatures close to melting. The different phases observed in this case are reported in Table 6. In most of the post-melting XRD analyses, the phases corresponding to the initial material (presented in Table 5) were also observed in addition to the metastable ones quenched from the liquid.

This is certainly due to the difficulty to extract only melted material for XRD from a laser-treated sample. For clarity, these phases remaining from the fresh material are not reported in Table 6. The XRD analyses of the melted materials reveal a biphasic composition in many cases, probably due to an incomplete demixing of thorium and zirconium during quenching which would lead to one zirconium rich phase and one thorium rich phase. Both fluorite and tetragonal phase were observed, depending of the sample, in agreement with Raman observations. The main discrepancy is obtained for Th_{0.2}Zr_{0.8}O₂ compositions where XRD shows a single phase with fluorite structure while Raman clearly reveals also spectra characteristic of tetragonal phase. However, these two structures are closely related with $a_{\text{Tetr}} \approx a_{\text{F}}/\sqrt{2}$ and $c_{\text{Tetr}} \approx a_{\text{F}}$. If a and c parameter of tetragonal phase follow the equation $a_{\text{Tetr}} = c_{\text{Tetr}}/\sqrt{2}$, it becomes difficult to distinguish between the two phases through XRD. The difference between Raman and XRD observations can also be due to the different scale probed by these 2 techniques. Indeed, it is possible that local atomic configuration corresponds to the tetragonal structure but with a certain level of disorder (as suggested by broad Raman peaks) that produce on the long-range organization an average structure corresponding to fluorite structure.

Following this idea, melting of the materials seems also to have a strong effect on the phase equilibria, probably due to segregation effects, since all the re-solidified samples have different lattice parameters. In the Th-rich compositions, a small fraction of metallic Th was observed, too (cf. Fig. 3).

Table 5

Lattice parameter of the different phases present in the sintered material (before melting).

Composition	Lattice parameters				
	Fm-3m (fcc) a/Å	P2 ₁ /c (mon) a/Å	b/Å	c/Å	β/°
ThO ₂	5.598(1)				
Th _{0.8} Zr _{0.2} O ₂	5.586(1)	5.164(1)	5.217(1)	5.328(1)	99.07(1)
Th _{0.6} Zr _{0.4} O ₂	5.586(1)	5.166(1)	5.218(1)	5.330(1)	99.10(1)
Th _{0.4} Zr _{0.6} O ₂	5.585(1)	5.165(1)	5.218(1)	5.330(1)	99.10(1)
Th _{0.2} Zr _{0.8} O ₂	5.586(1)	5.167(1)	5.218(1)	5.332(1)	99.09(1)
ZrO ₂		5.153(1)	5.207(1)	5.321(1)	99.21(1)

Table 6
Lattice parameters of the different phases present in material after melting experiment.

Composition	Lattice parameters/Å			Lattice parameters/Å		
	Molten in Ar <i>Fm-3m</i> (fcc) a	<i>P4₂/nmc</i> (tetr) a	c	Molten in air <i>Fm-3m</i> (fcc) a	<i>P4₂/nmc</i> (tetr) a	c
ThO ₂	5.598(1)			5.597(1)		
Th _{0.8} Zr _{0.2} O ₂	5.554(1)			5.560(1)		
				5.504(1)		
Th _{0.6} Zr _{0.4} O ₂	5.541(1)	3.629(1)	3.238(1)	5.493(1)		
				5.380(1)		
Th _{0.4} Zr _{0.6} O ₂	NA	NA		5.555(1)	3.629(1)	5.238(1)
Th _{0.2} Zr _{0.8} O ₂	5.229(1)			5.230(1)		

4. Discussion

4.1. Phase equilibria considerations

The present laser heating and pre- or post- melting characterisation highlights the excruciating experimental issues related to the investigation of the ThO₂-ZrO₂ system at very high temperature, up to and beyond its liquidus line. The main difficulties stem from the semi-transparency of both oxides, which makes it difficult to perform both laser heating and pyrometric temperature measurements on them; the vaporisation produced beyond 3000 K, which also hinders accurate optical measurements of the sample temperature; the segregation, upon cooling, of different phases, including cubic mixed oxides, tetragonal zirconia, and traces of metallic thorium. In this scenario, it is arduous to derive accurate phase diagram data from the present experimental investigation. Nonetheless, the current melting and solidification data show in an obvious manner, that a minimum melting point exists, in the pseudo-binary ThO₂-ZrO₂ plane, at an intermediate composition near Th_{0.4}Zr_{0.6}O₂ and a temperature of approximately 2750 K. This minimum melting point was never observed experimentally before the present investigation. In 1957, Duwez and Loh [17] performed melting experiments on mixed ZrO₂-ThO₂ oxides similar to those investigated in this work. They used a high-power solar furnace and obtained fast melting and quench on eleven mixed oxide compositions. However, the temperature of the melting and freezing materials was not directly measured. Therefore, the solid-liquid phase equilibria could only be estimated, in Ref. [17], from the crystal structures of the quenched samples. Yet, Duwez and Loh already estimated that a minimum melting temperature was likely to occur for $0.1 \leq x(\text{ThO}_2) \leq 0.4$. At that time, however, the existence of a high-temperature cubic allotropy of ZrO₂ was not yet known. Therefore, they assumed that the minimum melting temperature corresponded to a peritectic reaction, consistent with a miscibility gap, in the solidified material, between cubic ThO₂ and tetragonal ZrO₂. Only more recent research [32–34] established that the stable crystal structure of solid ZrO₂ near the melting point is cubic, isomorphic with CaF₂, and, therefore, completely soluble in ThO₂. Interestingly, the existence of a minimum melting temperature was foreseen also in the CALPHAD extrapolation, based on lower-temperature experimental data, performed by Kinoshita et al., in 2004 [9]. The present experimental results provide solidus and liquidus points in qualitative agreement with that CALPHAD optimisation, although they indicate that the minimum melting point occurs some 200 K lower and at a higher ThO₂ content with respect to Kinoshita's prediction (Fig. 4). Nonetheless, the agreement between the present data and the 2004 CALPHAD optimisation can still be seen as satisfactory, when one considers the large extrapolations on which the CALPHAD optimisation was based, due to complete lack of experimental data for the solid-liquid transition. It is also interesting to notice, that the minimum melting point

occurs at the same composition, and approximately also the same temperature, when the laser heating experiments are carried out under pressurised air or argon. In contrast, in the latter case (reducing conditions), a double inflection like in a liquidus-solidus solidification process was observed instead of the congruent melting/freezing transition displayed by the material in an oxidising atmosphere. This point suggests that oxygen defect formation most probably occurred for all the compositions, including the one melting at the minimum temperature, in a reducing environment, leading to the segregation of phases with different O/M ratio. Therefore, the solidus-liquidus lines reported in the ThO₂-ZrO₂ pseudo-binary plane are only projections of the corresponding three-dimensional surfaces, which better describe the solid-liquid transition in the ternary Th-Zr-O system.

Thermodynamically, oxygen losses can stabilise hypostoichiometric fcc zirconia at temperatures exceeding 1750 K [32]. Under certain conditions, the hypostoichiometric dioxide can be quenched as a lower-temperature metastable phase [33–37]. However, stoichiometric tetragonal or monoclinic zirconia coexisting with slightly oxidised zirconium (like for example the Zr₃O phase [34–36]) are the thermodynamic equilibrium phases at temperatures below 1700 K. A similar behaviour has been observed in the binary thorium-oxygen system, where it is, however, practically impossible to stabilise a hypostoichiometric dioxide below 3000 K [10,25]. At lower temperatures, stoichiometric fcc ThO₂ coexists with metallic thorium. For this reason, a study similar to the cation-valence investigation recently published by Mastromarino et al. [26], for the U-Zr-O system, is useless as a means to determine the final oxygen-to-metal ratio of laser melted and quenched samples in the Th-Zr-O system. In the Th-Zr-O system, due to the practically absolute stability of 4+ cations at room temperature and up to temperatures comparable with the melting point, oxygen losses occurring at very high temperature around the melting transitions result in demixing of pure or slightly oxidised Th and Zr when the material is quenched. Metallic Th was in fact observed in the present work by XRD analysis performed on melted and quenched samples.

4.2. Comparison with other mixed oxide systems

It is interesting to compare the ThO₂-ZrO₂ pseudo-binary phase diagram with those of other mixed dioxides recently investigated with the same experimental arrangement [12]. In both the UO₂-ThO₂ and PuO₂-ThO₂ pseudo-binary systems, a minimum melting point was observed by Latta et al. [38] and by Böhrer et al. [12] for ThO₂ concentrations lower than 10 mol %. In the UO₂-ThO₂ system, such behaviour was explained with the help of a thermodynamic assessment of both the fcc and the liquid phases, indicating a larger stability domain for the liquid phase at low concentrations of ThO₂. In the phase equilibria optimised by Kim [39], the broad miscibility gap in the solid dioxide at intermediate ThO₂ contents played an

important role in the determination of the Gibbs free energy of the fcc phase. The existence of such a miscibility gap was recently observed with quantum–mechanical calculations and Monte-Carlo simulations in nano-structured thorium-uranium mixtures [40]. However, these computational results still need to be experimentally corroborated. In contrast, the existence of a minimum melting point in the $\text{UO}_2\text{-ThO}_2$ and $\text{PuO}_2\text{-ThO}_2$ pseudo-binary systems is in excellent agreement with recent molecular dynamic simulations [41], where such behaviour is attributed to the formation of defects in the oxygen sublattice of the fluorite-like crystal structure close to melting.

These results give some hints about the possible trend of free energy curves characteristic of the phases occurring in the $\text{ThO}_2\text{-ZrO}_2$ system studied in this work. As already reported by Kinoshita [9], in the present system thorium and zirconia are largely immiscible in the solid state, at least up to the temperatures at which cubic ZrO_2 is stabilised with respect to tetragonal ZrO_2 . In this scenario, the Gibbs free energy of the fcc phase exceeds that of the liquid in a broad range of intermediate compositions, where a minimum melting point occurs. The solidus and liquidus lines remain rather flat and close to each other around the minimum melting point, in a pretty large compositional range. With respect to Kinoshita's extrapolation, the present data essentially update the position of the minimum melting point. This behaviour is qualitatively similar to the pseudo-binary $\text{UO}_2\text{-ZrO}_2$ system studied by Quaini et al. [36], Piluso et al. [42], Barrachin et al. [43] and Mastromarino et al. [26]. In particular, the minimum melting point occurs here at a composition, $x(\text{ThO}_2) = 0.4$, which is approximately the same zirconia concentration as the one established for the lowest melting in the $\text{UO}_2\text{-ZrO}_2$ system. However, surprisingly the minimum melting temperature, 2750 K, is lower here than the minimum melting point found in the uranium-zirconia system. The thermodynamic explanation of this result should probably be sought in the energetic effect of mixing large fractions of Zr^{4+} and Th^{4+} anions in the fcc and liquid phases. Moreover, the much larger difference between the melting points of ThO_2 and ZrO_2 , compared to that between the melting temperatures of uranium and zirconia, results in solidus and liquidus lines being much steeper and further apart in the ThO_2 -rich part of the pseudo-binary dioxide plane.

It is finally important, if somewhat obvious, to remark that the solid-liquid transition behaviour has been observed to be little influenced by the experimental atmosphere (oxidising or reducing) in the $\text{ThO}_2\text{-ZrO}_2$ system compared to the $\text{UO}_2\text{-ZrO}_2$ system. In the latter, uranium can be rather easily oxidised to U^{5+} and U^{6+} in the presence of oxygen at high temperature, promptly leading to the formation of higher oxides (like M_4O_9 or M_3O_8) displaying a much lower melting point outside the pseudo-binary plane [44]. In the present $\text{ThO}_2\text{-ZrO}_2$ system, instead, no change in the minimum melting point was observed by varying the experimental atmosphere, besides a more marked separation between the solidus and liquidus lines. This separation between solidus and liquidus in the $\text{ThO}_2\text{-ZrO}_2$ system seems to be less dangerous, in terms of fuel safety, compared to the over 300 K solidus point depression due to uranium over-oxidation observed in the uranium-zirconia system in the presence of air [26].

5. Conclusions

New laser heating results on the melting transition assist the assessment of the high temperature phase diagram of $\text{ThO}_2\text{-ZrO}_2$. Similarities and differences from the other pseudo-binary systems including thorium and zirconia have been indicated. The effects of an inert/reducing or oxidising atmosphere are less visible in this system thanks to the high stability of thorium. A minimum in the melting temperatures was recorded around 2750 K for a

composition near $\text{Th}_{0.4}\text{Zr}_{0.6}\text{O}_2$. The solid-liquid transition behaviour is barely influenced by the experimental atmosphere (oxidising or reducing) in the $\text{ThO}_2\text{-ZrO}_2$ system compared to that of $\text{UO}_2\text{-ZrO}_2$. In the present $\text{ThO}_2\text{-ZrO}_2$ system no change in the minimum melting point was observed by varying the experimental atmosphere. The only difference in the melting behaviour observed under reducing conditions consisted in a more marked separation between the solidus and liquidus lines, also at the minimum melting point, certainly due to the formation of oxygen-defect-rich zirconia at high temperature. This effect can be certainly considered as much more benign, in terms of fuel safety, compared to the huge melting point depression due to uranium over-oxidation studied in the uranium-zirconia system in the presence of air [26].

Material characterization performed before and after melting by SEM, Raman spectroscopy and XRD permitted the identification of different phases in sintered and molten materials. The observed coexistence of monoclinic zirconia and cubic thorium, in samples sintered and then cooled to room temperature, confirm that thorium under these conditions cannot stabilise the tetragonal phase of zirconia, unlike that reported in uranium-rich compositions for the system $\text{UO}_2\text{-ZrO}_2$. In contrast, tetragonal zirconia was observed by XRD and Raman spectroscopy to coexist with cubic ThO_2 and monoclinic ZrO_2 in samples quenched from the liquid phase in laser-heating experiments.

Acknowledgements

S.M. acknowledges the EURATOM FP7 project GENTLE (contract number 323304) for supporting her stay at JRC Karlsruhe.

Appendix A. Supplementary data

Supplementary data to this article can be found online at <https://doi.org/10.1016/j.jnucmat.2019.04.035>.

References

- [1] P.R. Hania, F.C. Klaassen, 3.04 - thorium oxide fuel, in: R.J.M. Konings (Ed.), *Compr. Nucl. Mater.*, Elsevier, Oxford, 2012, pp. 87–108. <https://doi.org/10.1016/B978-0-08-056033-5.00052-5>.
- [2] J. Belle, R. Berman, *Thorium Dioxide: Properties and Nuclear Applications*, Tech. rep., USDOE Office of Nuclear Energy, Science and Technology (NE), Jan. 1984. <https://doi.org/10.2172/5986642>.
- [3] J. Herring, P.E. MacDonald, K.D. Weaver, C. Kullberg, Low cost, proliferation resistant, uranium–thorium dioxide fuels for light water reactors, *Nucl. Eng. Des.* 203 (1) (2001) 65–85. [https://doi.org/10.1016/S0029-5493\(00\)00297-1](https://doi.org/10.1016/S0029-5493(00)00297-1).
- [4] M. Basu (Ali), R. Mishra, S. Bharadwaj, D. Das, Thermodynamic and transport properties of thorium–uranium fuel of advanced heavy water reactor, *J. Nucl. Mater.* 403 (1–3) (2010). <https://doi.org/10.1016/j.jnucmat.2010.01.009>.
- [5] C. Lombardi, L. Luzzi, E. Padovani, F. Vettraino, Inert matrix and thorium fuels for plutonium elimination, *Prog. Nucl. Energy* 38 (3–4) (2001) 395–398. [https://doi.org/10.1016/S0149-1970\(00\)00143-8](https://doi.org/10.1016/S0149-1970(00)00143-8).
- [6] C. Lombardi, L. Luzzi, E. Padovani, F. Vettraino, Thorium and inert matrix fuels for a sustainable nuclear power, *Prog. Nucl. Energy* 50 (8) (2008) 944–953. <https://doi.org/10.1016/j.pnucene.2008.03.006>.
- [7] W.E. Lee, M. Gilbert, S.T. Murphy, R.W. Grimes, Opportunities for advanced ceramics and composites in the nuclear sector, *J. Am. Ceram. Soc.* 96 (7) (2013) 2005–2030. <https://doi.org/10.1111/jace.12406>.
- [8] S.F. Ashley, G.T. Parks, W.J. Nuttall, C. Boxall, R.W. Grimes, Nuclear energy: thorium fuel has risks, *Nature* 492 (7427) (2012) 31–33. <https://doi.org/10.1038/492031a>.
- [9] H. Kinoshita, D. Setoyama, Y. Saito, M. Hirota, K. Kurosaki, M. Uno, S. Yamanaka, Thermodynamic modelling and phase stability assessment of MO_{2-x} oxides with a fluorite structure, *J. Chem. Thermodyn.* 35 (5) (2003) 719–731. [https://doi.org/10.1016/S0021-9614\(03\)00002-8](https://doi.org/10.1016/S0021-9614(03)00002-8).
- [10] R. Benz, Thorium–thorium dioxide phase equilibria, *J. Nucl. Mater.* 29 (1969) 43–49. [https://doi.org/10.1016/0022-3115\(69\)90125-1](https://doi.org/10.1016/0022-3115(69)90125-1).
- [11] C. Ronchi, J.P. Hiernaut, Experimental measurement of pre-melting and melting of thorium dioxide, *J. Alloy. Comp.* 240 (1996) 179–185. [https://doi.org/10.1016/0925-8388\(96\)02329-8](https://doi.org/10.1016/0925-8388(96)02329-8).
- [12] R. Böhler, A. Quaini, L. Capriotti, P. Çakır, O. Beneš, K. Boboridis, A. Guiot, L. Luzzi, R.J.M. Konings, D. Manara, The solidification behaviour of the $\text{UO}_2\text{-ThO}_2$ system in a laser heating study, *J. Alloy. Comp.* 616 (2014) 5–13. <https://doi.org/10.1016/j.jnucmat.2014.04.035>.

- doi.org/10.1016/j.jallcom.2014.07.055.
- [13] C. Guéneau, A. Chartier, L.V. Brutzel, Thermodynamic and thermophysical properties of the actinide oxides, in: R.J.M. Konings (Ed.), *Compre. Nucl. Mater, first ed.*, Elsevier, Amsterdam, 2012.
- [14] D. Manara, L. Soldi, S. Mastromarino, K. Boboridis, D. Robba, L. Vlahovic, R. Konings, Laser-heating and radiance spectrometry for the study of nuclear materials in conditions simulating a nuclear power plant accident, *J. Vis. Exp.* 130 (2017) (2017) e54807, <https://doi.org/10.3791/54807>.
- [15] R. Böhler, M.J. Welland, F. De Bruycker, K. Boboridis, A. Janssen, R. Eloirdi, R.J.M. Konings, D. Manara, Revisiting the melting temperature of NpO_2 and the challenges associated with high temperature actinide compound measurements, *J. Appl. Phys.* 111 (2012) 113501. <https://doi.org/10.1063/1.4721655>.
- [16] O. Cedillos-Barraza, D. Manara, K. Boboridis, T. Watkins, S. Grasso, D.D. Jayaseelan, R. Konings, M. Reece, W. Lee, Investigating the highest melting temperature materials: a laser melting study of the TaC-HfC system, *Sci. Rep.* 6 (2016), <https://doi.org/10.1038/srep37962>, 379621–11.
- [17] P. Duwez, E. Loh, Phase relationships in the system zirconia—thoria, *J. Amer. Ceram. Soc.* 40 (1957) 321–324. <https://doi.org/10.1111/j.1151-2916.1957.tb12629.x>.
- [18] V. Tyrpekl, M. Holzhäuser, H. Hein, J.-F. Vigier, J. Somers, P. Svora, Synthesis of dense yttrium-stabilised hafnia pellets for nuclear applications by spark plasma sintering, *J. Nucl. Mater.* 454 (2014) 398–404. <http://doi.org/10.1016/j.jnucmat.2014.08.029>.
- [19] D. Manara, R. Böhler, L. Capriotti, A. Quaini, Z. Bao, K. Boboridis, L. Luzzi, A. Janssen, P. Pöml, R. Eloirdi, R.J.M. Konings, On the melting behaviour of calcium monoxide under different atmospheres: a laser heating study, *J. Eur. Ceram. Soc.* 34 (2014) 1623–1636. <https://doi.org/10.1016/j.jeurceramsoc.2013.12.018>.
- [20] M.J. Welland, R. Böhler, L. Vlahovic, K. Boboridis, D. Manara, Co-development of experimental and simulation methods for the laser flash heating and melting technique: the thermoelastic effects of UO_2 , *Int. J. Therm. Sci.* 132 (2018) 174–185. <https://doi.org/10.1016/j.ijthermalsci.2018.05.035>.
- [21] L. Capriotti, A. Quaini, R. Böhler, K. Boboridis, L. Luzzi, D. Manara, A laser heating study of the CeO_2 solid/liquid transition: challenges related to a refractory compound with a very high oxygen pressure, *High Temp.–High Press* 44 (2014) 69–82. ISSN: 00181544.
- [22] V. Petříček, M. Dusek, L. Palatinus, Crystallographic computing system JANA2006: general features, *Z. fur Kristallogr.* 229 (2014) 345–352.
- [23] H. Richter, Z. Wang, L. Ley, The one phonon Raman spectrum in microcrystalline silicon, *Solid State Commun.* 39 (1981) 625, [https://doi.org/10.1016/0038-1098\(81\)90337-9](https://doi.org/10.1016/0038-1098(81)90337-9).
- [24] D. Manara, M. Sheindlin, W. Heinz, C. Ronchi, New techniques for high-temperature melting measurements in volatile refractory materials via laser surface heating, *Rev. Sci. Instrum.* 79 (2008) 113901–113909. <https://doi.org/10.1063/1.3005994>.
- [25] A. Bergeron, D. Manara, O. Beneš, R. Eloirdi, M.H.A. Piro, E.C. Corcoran, Thermodynamic modelling of thoria-urania and thoria-plutonia fuels: description of the Th-U-Pu-O quaternary system, *J. Nucl. Mater.* 512 (2018) 324–348. <https://doi.org/10.1016/j.jnucmat.2018.09.013>.
- [26] S. Mastromarino, A. Seibert, E. Hashem, A. Ciccio, D. Prieur, A. Scheinost, S. Stohr, P. Lajarge, J. Boshoven, D. Robba, M. Ernstberger, D. Bottomley, D. Manara, Assessment of solid/liquid equilibria in the (U, Zr) O_2 +y system, *J. Nucl. Mater.* 494 (2017) 368–379. <https://doi.org/10.1016/j.jnucmat.2017.07.045>.
- [27] T. Shimanouchi, M. Tsuboi, T. Miyazawa, Optically active lattice vibrations as treated by the GF-Matrix method, *J. Chem. Phys.* 35 (1961) 1597. <https://doi.org/10.1063/1.1672186>.
- [28] V.G. Keramidas, W.B. White, Raman spectra of oxides with the fluorite structure, *J. Chem. Phys.* 59 (1973) 1561. <https://doi.org/10.1063/1.1680227>.
- [29] D.P.C. Thackeray, The Raman spectrum of Zirconium dioxide, *Spectrochim. Acta* 80 (1973) 550–551.
- [30] V.G. Keramidas, W.B. White, Raman scattering study of the crystallization and phase transformations of ZrO_2 , *J. Amer. Ceram. Soc.* 57 (1973) 22–24.
- [31] B.-K. Kim, J.-W. Hahn, K.R. Han, Quantitative phase analysis in tetragonal-rich tetragonal/monoclinic two phase zirconia by Raman spectroscopy, *J. Mat. Res. Lett.* 16 (1997) 669–671.
- [32] R.J. Ackerman, E.G. Rauh, C.A. Alexander, The thermodynamic properties of $\text{ZrO}_2(\text{g})$, *High Temp. Sci.* 7 (1975) 304–316.
- [33] R.J. Ackerman, S.P. Garg, E.G. Rauh, The lower phase boundary of ZrO_2 , *J. Am. Ceram. Soc.* 61 (1978) 275–276.
- [34] R. Arroyave, L. Kaufman, T.W. Eagar, Thermodynamic modelling of the Zr-O system, *Calphad* 26 (2002) 95–118.
- [35] A. Quaini, Etude thermodynamique du corium en cuve - Application a l'interaction corium/beton, Ph. D. Thesis presented at the University of Grenoble Alpes, 2016.
- [36] A. Quaini, C. Guéneau, S. Gossé, N. Dupin, B. Sundman, E. Brackx, R. Domenger, M. Kurata, F. Hodaj, Contribution to the thermodynamic description of the corium – the U-Zr-O system, *J. Nucl. Mater.* 501 (2018) 104–131. <https://doi.org/10.1016/j.jnucmat.2018.01.023>.
- [37] R. Böhler, P. Çakır, O. Beneš, H. Hein, R.J.M. Konings, D. Manara, High temperature phase transition of mixed PuO_2 – ThO_2 investigated by laser melting, *J. Chem. Thermodyn.* 81 (2015) 245–252. <https://doi.org/10.1016/j.jct.2014.10.006>.
- [38] R. Latta, E. Duderstadt, R. Fryxell, Solidus and liquidus temperatures in the UO_2 – ThO_2 system, *J. Nucl. Mater.* 35 (1970) 347–349. [https://doi.org/10.1016/0022-3115\(70\)90219-9](https://doi.org/10.1016/0022-3115(70)90219-9).
- [39] J. Kim, S.S. Kim, Thermodynamic modelling of the UO_2 – ThO_2 phase diagram, *Model. Simulat. Mater. Sci. Eng.* 24 (2016), 0250101–9, <https://doi.org/10.1088/0965-0393/24/2/025010>.
- [40] L.C. Shuller, R.C. Ewing, U. Becker, Thermodynamic properties of $\text{Th}_x\text{U}_{1-x}\text{O}_2$ ($0 < x < 1$) based on quantum–mechanical calculations and Monte-Carlo simulations, *J. Nucl. Mater.* 412 (2011) 17–25. <https://doi.org/10.1016/j.jnucmat.2011.01.017>.
- [41] P.S. Ghosh, N. Kuganathan, C.O.T. Galvin, A. Arya, G.K. Dey, B.K. Dutta, R.W. Grimes, Melting behavior of $(\text{Th,U})\text{O}_2$ and $(\text{Th,Pu})\text{O}_2$ mixed oxides, *J. Nucl. Mater.* 479 (2016) 112–122. <https://doi.org/10.1016/j.jnucmat.2016.06.037>.
- [42] P. Piluso, G. Trillon, C. Journeau, The UO_2 – ZrO_2 system at high temperature ($T > 2000$ K): importance of the meta-stable phases under severe accident conditions, *J. Nucl. Mater.* 344 (2005) 259e264. <https://doi.org/10.1016/j.jnucmat.2005.04.052>.
- [43] M. Barrachin, P.Y. Chevalier, B. Cheynet, E. Fischer, New modelling of the U-O-Zr phase diagram in the hyper-stoichiometric region and consequences for the fuel rod liquefaction in oxidising conditions, *J. Nucl. Mater.* 375 (2008) 397–409. <https://doi.org/10.1016/j.jnucmat.2008.02.003>.
- [44] C. Guéneau, A. Chartier, L. Van Brutzel, Thermodynamic and Thermophysical properties of the actinide oxides, in reference module in materials science and materials engineering, *Compr. Nucl. Mater.* 2 (2012) 21e59. <https://doi.org/10.1016/B978-0-08-056033-5.00009-4>.